Lab on a Chip

ROYAL SOCIETY OF CHEMISTRY

PAPER

View Article Online
View Journal | View Issue

Check for updates

Cite this: *Lab Chip*, 2022, **22**, 2185

A graphene oxide scaffold-encapsulated microcapsule for polysulfide-immobilized long life lithium–sulfur batteries†

Xirong Lin,‡[a] Chaoyu Yang,‡[b] Tianli Han,[c] Jinjin Li, *[a] Zhonghua Chen,*[d] Haikuo Zhang, [a] Kai Mu,[b] Ting Si *[b] and Jinyun Liu *[c]

Received 18th February 2022,
Accepted 28th April 2022

DOI: 10.1039/d2lc00161f

rsc.li/loc

Engineering high-performance cathodes for high energy-density lithium–sulfur (Li–S) batteries is quite significant to achieve commercialization. Here, we develop a graphene oxide scaffold/sulfur composite-encapsulated microcapsule (GSM) for high-performance Li–S batteries, which is prepared through the co-flow focusing (CFF) approach. The GSM-based cathode displays a high capacity of 1004 mA h g^{-1} at 0.2C after cycling 200 times, a long-term cycling stability after 1000 cycles at 2C, and a good rate-performance. At temperatures of −5 °C and 45 °C, the electrochemical performance is also excellent. The computational calculations based on density functional theory (DFT) verify the high adsorption energies of the microcapsules towards polysulfides, suppressing the shuttle effect efficiently. It is expected that the GSM system developed based on the CFF method here and its high electrochemical performance will enable it to be applicable for preparing many other emerging energy-storage materials and secondary batteries.

1. Introduction

Lithium–sulfur (Li–S) batteries are considered to be promising next-generation power batteries because of their high theoretical energy-density, which is highly significant for electrical vehicles.[1–3] Currently, practical commercialization is severely restricted by some issues including the large volume-change of sulfur, and the shuttle effect.[4–8] Improving the electrochemical properties needs mechanically-robust and chemically-stable cathodes, which accommodate the volume-change, suppress the loss of polysulfides, and provide continuous pathways for the transport of both electrons and ions.[9–12] These make the preparation of high-performance cathodes quite challenging. Previous studies have shown some efficient strategies.[13–16] For example, carbon-based nanomaterials have been widely used in Li–S batteries.[17–19] Their spherical structure and small size are important for improving the tap density; while their high conductivity benefits the transfer of electrons. Moreover, micro–mesopores and voids inside the sulfur hosts are able to increase the loading and accommodate the volume-change, respectively.[20,21]

Among various carbon-based sulfur hosts, graphene has good potential because of its high specific surface area, mechanical strength, good conductivity and flexibility.[22,23] Cao *et al.* coated nano-sulfur on graphene oxide sheets (GOSs) by using a redox reaction between sodium thiosulfate and hydrochloric acid, which exhibited stable electrochemical performance.[24] However, developing a well-controllable preparation approach for engineering specific graphene oxide (GO)-based sulfur hosts to achieve volume-change accommodating, conductive, and polysulfide-immobilizing performances simultaneously is needed.

Here, we present a microcapsule system encapsulated with a three-dimensional (3D) GO scaffold inside as a high-performance sulfur host. The microcapsules are prepared through a well-controllable microfluidic method named co-flow focusing (CFF), in which coaxial liquid jets are issued from the tip of the steady liquid cone and core–shell structured droplets can be formed due to the instability mechanism.[25,26] Different from traditional microfluidic methods such as planar microchannels and glass microcapillaries, the CFF process enables massive production of microcapsules by a hundred fold with narrow size distribution and wide material

---

[a] *National Key Laboratory of Science and Technology on Micro/Nano Fabrication, Key Laboratory for Thin Film and Microfabrication of Ministry of Education, Department of Micro/Nano-electronics, Shanghai Jiao Tong University, Shanghai 200240, PR China. E-mail: lijinjin@sjtu.edu.cn*

[b] *Department of Modern Mechanics, University of Science and Technology of China, Hefei, Anhui 230026, PR China. E-mail: tsi@ustc.edu.cn*

[c] *Key Laboratory of Functional Molecular Solids of Ministry of Education, Anhui Provincial Engineering Laboratory for New-Energy Vehicle Battery Energy-Storage Materials, College of Chemistry and Materials Science, Anhui Normal University, Wuhu, Anhui 241002, PR China. E-mail: jyliu@ahnu.edu.cn*

[d] *Shenzhen FBTech Electronics Ltd., Shenzhen, Guandong 518100, PR China. E-mail: chenzhonghua@fbwtt.com*

† Electronic supplementary information (ESI) available: Supplementary figures and movies. See DOI: **https://doi.org/10.1039/d2lc00161f**

‡ These authors contribute equally to this work.

combinations.[27,28] Moreover, the CFF device can overcome the viscous effects and avoid the capillarity and wetting effects of device boundary walls. It is beneficial for the solidification of microcapsules in post processing, and further scaling up by replicating the coaxial needles in an industrial setting. After sulfur infiltration, sulfur was loaded onto the 3D GO scaffold, finally forming 3D GO/S composite-infilled microcapsules (GSMs). The GSM-based Li–S battery cathode would possess the following features: i) the 3D GO scaffold core effectively enhances the conductivity, improving the electron transfer of the overall system, and the abundant functional groups on GO capture polysulfides; ii) GMs have a high specific surface area, which enables a high sulfur loading not only suppressing the aggregation of sulfur species, but also accommodating the volumetric expansion during lithiation; iii) the porous carbon shell is beneficial for electrolyte penetration, and it would also be a physical constraint for the transport of polysulfides. On the basis of these advantages, the GMSs display an excellent capacity of 1004 mA h g^{-1} after 200 cycles, and a long cycling life of 1000 cycles at 2C. High rate-performance and good temperature-tolerance are also achievable. The density functional theory (DFT)-based calculations were also conducted, which showed the high adsorption energies of the microcapsule system towards polysulfides for efficiently suppressing the shuttle effect.

2. Experimental section

2.1. Preparation of the GO-encapsulated microcapsules (GMs)

In a typical microfluidic process, the coaxial needle comprised of two needles including the inner needle: inner diameter (d_i) = 0.26 mm, outer diameter (d_o) = 0.49 mm; and outer needle: d_i = 0.84 mm, d_o = 1.27 mm, which are coaxially nested together by laser welding. It is noted that the coaxial needle was assembled concentrically, thereby ensuring a steady fluid supply and uniform flow field. Then it was fixed in a polymethyl methacrylate (PMMA) chamber with a cork. The bottom of the chamber was sealed with a thin glass slide with an orifice (0.3 mm) at the center. The tip of the inner needle was protruded 0.2 mm more than the outer needle.

Three syringe pumps (Suzhou Xunfei Scientific Instrument Co. LTD, XF-101P) were employed to provide a stable flow to the corresponding channels of the device. First, GO was prepared through the conventional Hummers' method. Then, the resultant GO aqueous solution (4 mg mL^{-1}) was typically used as the inner core liquid; and a poly(vinyl alcohol) aqueous solution (2 wt%) was used as the focusing liquid. And the photocurable monomer ethoxylated trimethylolpropane triacrylate (ETPTA) mixed with 2% photo-initiator 2-hydroxy-2-methylphenyl propanone (HMPP) was employed as the outer shell liquid. An appropriate amount of ethanol was added as an additional solvent to ensure good mixing. The mixture was heated to accelerate and ensure the complete volatilization of ethanol. In our study, the flow rates of the inner phase (Q_i), outer phase (Q_o), and focusing phase (Q_f) were optimized to be Q_i = 3 mL h^{-1}, Q_o = 4 mL h^{-1}, and Q_f = 700 mL h^{-1}, respectively. The system produced about 10 000 microcapsules per minute. A horizontal microscope lens with a charge coupled device (CCD) camera (The Imaging Source, DFK-23G274) was employed to observe the real-time dynamics during microcapsule preparation. A strobe flashlight (Hangzhou Pintuo Electronic Technology Co. LTD, flashing frequency: 3000 Hz) was employed for illumination. The resultant droplets were received in a collector and solidified by UV light (De Sheng Xing Electronics Co. Ltd., UVP60, 8.8 W cm^{-2}) for 5 min of radiation. The collected droplets were then washed three times with deionized water. Lastly, after drying by sublimation using an LGJ-10 vacuum freeze-dryer for 2 days, the microcapsules were calcined at 500 °C under an ultrapure N_2 atmosphere for 2 h. The obtained samples were named as GMs-H and GMs for GO solution concentrations of 4 and 1 mg mL^{-1} during encapsulation, respectively.

2.2. Preparation of GO/S-encapsulated microcapsules

GSMs-H was obtained by a melt-diffusion method. Firstly, we mixed GMs-H and commercial sulfur powders with a mass ratio of 1 : 4 and baked the mixture in a tube furnace at 155 °C for 15 h in nitrogen gas. Then, the surface residual sulfur of the microcapsules was removed by rapid heat-treatment at 200 °C for 30 min. Moreover, sulfur was also coated onto GO sheets (GSs) directly, forming a sample named as GSSs.

2.3. Characterization

The morphology was characterized by using an atomic force microscope (AFM, Veeco MultiMode V), a scanning electron microscope (SEM, Hitachi S-4800) with an energy dispersive spectrometer (EDS), a transmission electron microscope (TEM, Hitachi HT7700), and an optical microscope (Nikon ECLIPSE Ts2). The structure and composition information were investigated by X-ray diffraction (XRD, Bruker D8 Advance) and X-ray photoelectron spectroscopy (XPS, Thermo-VG Scientific ESCALAB 250Xi). The sulfur loading in the cathode was measured by thermogravimetric analysis (TGA, Perkin-Elmer, Pyris 1) in an air flow with a ramp rate of 10 °C min^{-1}. N_2 adsorption–desorption isotherms of the microcapsules were recorded on a Tristar II 3020 M system. Raman spectra were recorded on a LabRAM HR800 (Horiba) using a 532 nm Nd:YAG laser excitation source. Characterization of GO nanosheets for dynamic light scattering and zeta potential was performed on a Malvern Zetasizer Nano ZS90.

2.4. Electrochemical tests

To prepare the cathode, the microcapsules, poly-vinylidene fluoride (PVDF) and carbon black (weight ratio = 8 : 1 : 1) were mixed in *N*-methylpyrrolidone (NMP). A slurry was formed, and coated on Al foil, and then dried in a vacuum chamber, formed into 12 mm diameter-disks subsequently. The electrolyte contained 1.0 M lithium bis-trifluoromethanesulfonimide (LiTFSI) in 1,2-dimethoxyethane and 1,3-dioxolane (volumetric ratio = 1 : 1) with 0.1 M $LiNO_3$. The loadings of sulfur in GSMs-H and GSMs were approximately 1.24 and 1.07 mg cm^{-2}, and the electrolyte/S ratios were about 21.3 and 24.6 μL mg^{-1}, respectively. Celgard-2400 film was employed as the separator. The 2032-type coin cells were assembled in an argon-filled glove box (Mikrouna Super 1220/750). Galvanostatic charge–discharge was tested on a Neware CT-4008 battery tester system. Cyclic voltammetry (CV) curves were recorded in an electrochemical workstation (CHI-660E). Electrochemical impedance spectra (EIS) were also obtained from the same equipment in a frequency range between 10 mHz and 100 kHz. Measurements at low/high temperatures (−5 °C and 45 °C) were conducted in a temperature thermotank (BTC-4010, Biolab Equipment Co., Ltd).

2.5. Adsorption measurement towards polysulfides

A Li_2S_6 solution was firstly synthesized by the reaction between sublimed sulfur and Li_2S (molar ratio = 5 : 1) in 50 mL of DME. It was vigorously stirred at 70 °C for several days under argon gas. 20 mg of GMs-H was added into a Li_2S_6 solution (4 mL), the mixture was left in a glove box overnight. The capability for absorbing polysulfides was evaluated by UV-vis spectroscopy (LAMBDA 850).

2.6. Computational calculation

The binding energies between carbon and polysulfides were calculated with the Vienna *ab initio* simulation package using a DFT method. A projector augmented wave method was used. The exchange correlation functional of generalized gradient approximation (GGA) with the Perdew–Burke–Ernzerhof (PBE) method was adopted. Single layer carbon atoms were cleaved to imitate the real carbon materials with a vacuum layer thickness of 15 Å. And the convergence criteria were set as 1 × 10^{-6} eV atom^{-1} and 0.01 eV Å^{-1}, respectively. A cut-off energy of 550 eV and a *K*-grid of 3 × 3 × 1 were used. Lastly, the binding energy was obtained by the formula: $E_b = E_t - E_C - E_p$, where E_t, E_C, and E_p were the energies of polysulfides on the carbon layer, carbon, and polysulfides, respectively.

3. Results and discussion

Fig. 1a illustrates the preparation of the microcapsules by the CFF approach. On the basis of the instability of the flows, the focusing coaxial jet breaks into microdroplets, resulting in the inner phase (GO solution) being encapsulated by the outer phase.[29–31] In the CFF system, one syringe contained a certain concentration GO aqueous solution as the inner phase, another syringe contained an organic photocurable oil phase which is used as the outer phase, and the third syringe was the focusing phase. During microfluidic preparation, when the Q_f attained the threshold, a coaxial cone liquid jet was generated which decomposed into core–shell microcapsules in view of flow instability. The samples containing the GO aqueous solution and shell precursor were solidified by ultraviolet illumination and freeze-drying followed by thermal-annealing treatment, forming a 3D GO scaffold-infilled microcapsule system. The real-time cone formation during preparation, and microdrops in the jet are displayed in ESI† Movie S1–S3. After that, the microcapsules were freeze-dried to form a GO scaffold inside. Finally, sulfur was coated through a sublimation–adsorption mechanism.

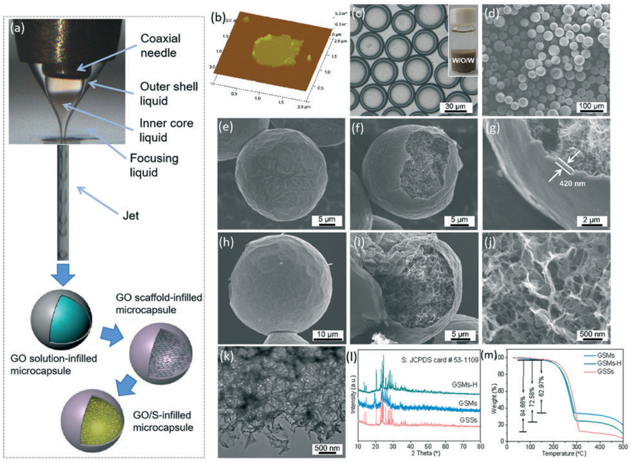

Fig. 1 (a) The cone-jet mode during microcapsule preparation. At the bottom, multiple steps for treating microcapsules are illustrated. (b) AFM image of a GO sheet. (c) Optical image of the microcapsules after UV-curing. The insert in (c) displays a vial of microcapsules. (d) SEM image of the microcapsules after UV-radiation. (e–g) SEM images of the microcapsules after carbonization (GMs-H). (h–j) SEM images of GSMs-H. (k) TEM image of the inner core of GSMs-H. (l) XRD patterns and (m) TGA profiles.

In the AFM images (Fig. 1b and S1, ESI†), the thickness of the GO sheet is ≈0.863 nm, indicating that it is approximately three layers thick. The zeta potential of GO nanosheets is −41.6 mV (Fig. S1e, ESI†), while the size-distribution is displayed in Fig. S1f (ESI†). In Fig. 1c and d and S2a (ESI†), the dark brown GO cores are encapsulated in the cured ETPTA shell after solidification by UV radiation. In the inset of Fig. 1c, a vial of collected microcapsules is displayed. The size-distribution (Fig. S2b, ESI†) displays that the microcapsules have a diameter of 30–40 μm. Fig. 1e and S2c (ESI†) show that the microcapsules retain the robust morphology after thermal treatment, forming microcapsules with a 3D GO scaffold as a core and carbonized polymer as a shell. A type-II profile in the N_2 adsorption–desorption isotherms is displayed in Fig. S2d (ESI†). The BET specific surface area is 182.7 m^2 g^{-1}, which is quite high, and facilitates the loading of sulfur. In addition, the mesopores provide pathways for Li$^+$ ion diffusion. Seen from a broken microcapsule (Fig. 1f and g and S2e–i, ESI†), GO sheets are observed. The microcapsule shell is approximately 400 nm, as presented in Fig. 1g. After loading sulfur (Fig. 1h–k and S3, ESI†), the microcapsules maintain the original shape.

In Fig. S4a–c (ESI†), mapping images present that sulfur is not obvious on the surface, and the signal of sulfur in the corresponding EDS spectrum (Fig. S4d, ESI†) is almost invisible. In contrast, Fig. S4e–g (ESI†) show the cross-sectional SEM and elemental mapping images of carbon and sulfur, verifying that the sulfur is located inside the microcapsules. The EDS spectrum (Fig. S4h, ESI†) indicates that sulfur has been coated into the microcapsules uniformly. In XRD patterns (Fig. 1l), diffraction peaks of sulfur are observed. As measured by TGA (Fig. 1m), the sulfur content in GSMs-H, GSMs with a lower graphene content (GSMs, Fig. S5, ESI†), and graphene oxide/sulfur sheets (GSSs, Fig. S6, ESI†) are 72.58%, 62.97%, and 84.66%, respectively.

In Fig. S7a (ESI†) the XPS survey spectrum shows the elements C, S and O of the microcapsules. The S 2p spectrum is shown in Fig. S7b (ESI†). S $2p_{3/2}$, S $2p_{1/2}$, and sulfate species are located at 163.8, 165.0, and 169.0 eV, respectively.[32] In Fig. S7c (ESI†), the peaks around 284.7 and 285.2 eV are ascribed to the sp^2 and sp^3 hybridized carbons, while others at 286.6, 288.4, and 289.1 eV are indexed to C–O, C=O and O–C=O, respectively.[33] In the Raman spectra (Fig. S8, ESI†), all samples show the D band at 1342 cm^{-1} and the G band at 1589 cm^{-1} of carbon, indicating the non-sp^2 and graphitic sp^2 stretching modes, respectively.[34] The I_D/I_G values of GMs-H and GSMs-H (Fig. S8a, ESI†), GMs and GSMs (Fig. S8b, ESI†), GSs and GSSs (Fig. S8c, ESI†) are similar, suggesting no significant difference of graphene oxide after loading sulfur.[35]

The microcapsules are controlled by adjusting the flow rates. The CFF process follows a scaling law, as $D \sim \alpha\,[(Q_i + Q_o)/Q_f]^{1/2}\cdot D_{orif}$,[36] where α is a constant associated with liquid properties; D and D_{orif} are the droplet and orifice diameters, respectively; Q_i, Q_o, and Q_f are the flow rates of the inner, outer and focusing phases, respectively. When the sum of Q_i and Q_o increases, the microcapsule diameter increases; while it decreases with the increase of Q_f as displayed in Fig. 2(1–6) and S9 (ESI†). When Q_i = 3 mL h^{-1}, Q_o = 4 mL h^{-1}, and Q_f = 300 mL h^{-1}, the diameter is about 127 μm. In contrast, when Q_f increases to 1100 mL h^{-1}, the diameter reduces to 62 μm. In Fig. 2(1–3) and S10 (ESI†), the flow rate Q_f is 700 mL h^{-1} and $Q_i = Q_o$. When $Q_i = Q_o$ increases to 4, 7, 10, 13, 16, 19, and 22 mL h^{-1}, the diameter increases. In Fig. 2(4–6) and S11 (ESI†), the flow rate for Q_i is 3 mL h^{-1}, and Q_o is 4 mL h^{-1}. When Q_f increases to 400, 500, 800, 900, 1100, 1300, and 1500 mL h^{-1}, the size reduces gradually.

The stability of inner and outer phases ($\varphi = Q_i/Q_o$) is shown in Fig. 2(7–9) and S12 (ESI†). When the microdroplets have one core, it follows: $d \sim [1 - Q_i^{1/3}/(Q_i + Q_o)^{1/3}]\cdot D$,[37] where d is the average shell thickness, D is the diameter of microcapsules, Q_i and Q_o are the flow rates of inner and outer phases, respectively. Fig. 2a(7–9) and S13 (ESI†) present the cone-jet changing with φ (1 : 15, 2 : 14, 3 : 13, 5 : 11, 7 : 9, 9 : 7, 11 : 5, 13 : 3, 15 : 1), when $Q_i + Q_o$ = 16 mL h^{-1} and Q_f = 700 mL h^{-1}. The microcapsules have one core only, when the flow rate ratio is large, as displayed in Fig. 2b. However, when the flow rate ratio is small, the microcapsules have multiple cores (Fig. 2b7 and S12b1, ESI†).

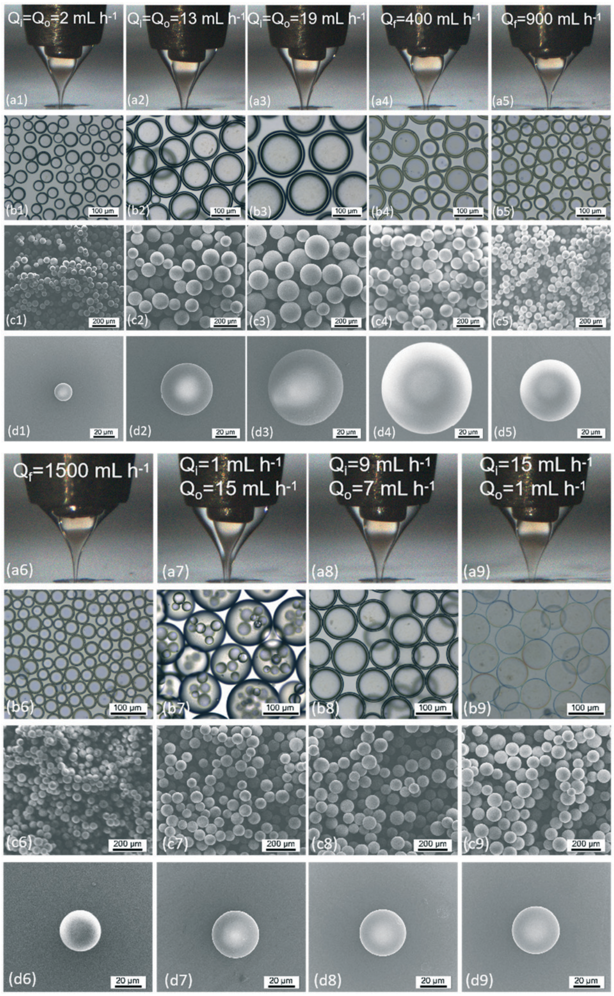

Fig. 2 (a) Steady cone-jet structure and (b) optical, (c and d) SEM images of microcapsules. The liquid flow rates are as follows: (1–3) $Q_i = Q_o$, Q_f = 700 mL h^{-1}; (4–6) Q_i = 3 mL h^{-1}, Q_o = 4 mL h^{-1}; (7–9) $Q_i + Q_o$ = 16 mL h^{-1}, Q_f = 700 mL h^{-1}.

Fig. 3a shows the CV curves of the GSMs-H Li–S batteries at 0.1 mV s^{-1}. The peak at 2.28 V is assigned to the reduction of S_8 to long-chain Li_2S_n ($4 \le n \le 8$). Another one at 2.02 V indicates the reduction of long-chain Li_2S_n to short-chain Li_2S_2 and Li_2S.[38] The anodic peak at 2.40 V is ascribed to the S_8 conversion from Li_2S_2 and Li_2S.[39] The almost overlapping CV profiles in the first-five cycles indicate a highly reversible electrochemical process. Fig. 3b presents the charge–discharge curves of the GSMs-H cathode at 0.2C. The plateau at 2.28 V is indexed to the S_8 ring opening;[40] while 2.02 V indicates the conversion of Li_2S_n to Li_2S_2/Li_2S.[41] GSMs-H provides an initial capacity of 1397 mA h g^{-1} which remains 1004 mA h g^{-1} after cycling 200 times, as displayed in Fig. 3c. In contrast, the GSMs and GSSs exhibit obvious capacity decay, indicating that a small content of graphene oxide nanosheets and a lack of shell protection are not ideal for a good electrochemical performance. Moreover, a robust structure is verified through the SEM images of the post-cycled microcapsules (Fig. S14, ESI†).

Fig. 3d shows the rate-performance cycling from 0.2C to 2.5C. The GSMs-H presents much better capacities compared to others, indicating good electrochemical dynamics for charging and discharging at different speeds. In addition, the high capacity remains stable after three rounds of cycling.

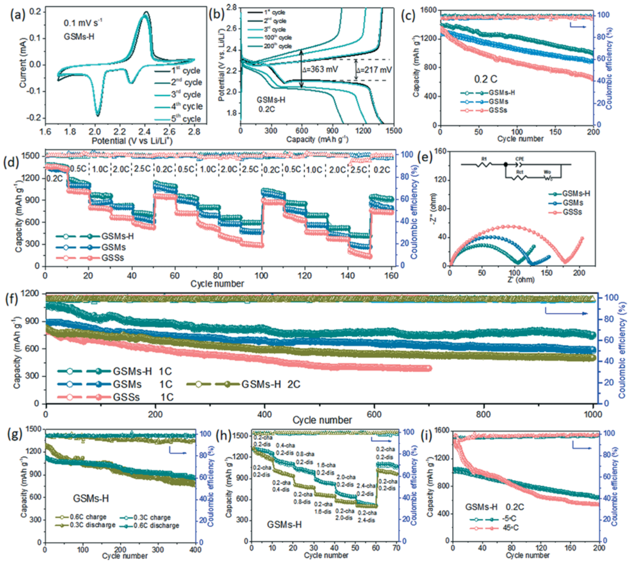

Fig. 3 (a) CV curves of the GSMs-H in the first-five cycles. (b) Charge–discharge profiles of GSMs-H at 0.2C. (c) Capacity of GSMs-H, GSMs and GSSs at 0.2C. (d) Rate-performance for three rounds. (e) Nyquist plots after 200 cycles at 0.2C. The equivalent circuit is shown in insers. (f) Cycling performance for 1000 cycles at 1C and 2C. (g) Cycling performance of GSMs-H at 0.6C charge *vs.* 0.3C discharge, and 0.3C charge *vs.* 0.6C discharge. (h) Rate-performances of GSMs-H when charging and discharging at different rates. (i) Cycling performance of GSMs-H at 45 °C and −5 °C.

This is ascribed to the special 3D porous scaffold-infilled microcapsule structure with efficient pathways for the transport of electrons and ions. Moreover, it is appropriate for accommodating the structural change of sulfur.[42] The stable and high conductivity of GSMs-H is verified by the EIS spectra (Fig. 3e). GSMs-H was also cycled 1000 times at 1C, as shown in Fig. 3f. The first-cycle capacity is 1100 mA h g^{-1}, and the capacity decay rate is 0.04% per cycle. After cycling 1000 times, the capacity and coulombic efficiency exceed 800 mA h g^{-1} and 98.2%, which are competitive with some reported studies about GO-based sulfides (Table S1, ESI†). In Fig. 3g, when the charge/discharge rate is 0.3C/0.6C, GSMs-H shows 867 mA h g^{-1} after 400 cycles; and the capacity is 809 mA h g^{-1} in the case of 0.6/0.3C. In Fig. 3h, when the discharge rate remains 0.2C, the capacity decreases with an increasing charge rate, along with good recoverability, indicating potential for practical applications.

The electrochemical performance of the Li–S batteries was also measured at −5 °C and 45 °C to evaluate their potential applications (Fig. 3i). At −5 °C, the capacity remains 645 mA h g^{-1} when cycling 200 times. The relatively low capacity could be caused by the slow reaction kinetics at a low temperature.[43] When cycling at 45 °C, the capacity is large at the initial period, which is attributed to the good activity at high temperature.[44] The capacity decreases in the following charge–discharge cycles, which is perhaps because of the electrolyte instability.[45] Considering the requirements of commercialization and further improving the energy density of Li–S battery systems, the sulfur loadings in GSMs-H were increased from 3.23 to 4.75 and 6.51 mg cm^{-2}, respectively. Fig. S15 (ESI†) shows the specific capacity of GSMs-H with large sulfur loadings at 0.2 C. With a high sulfur loading of 6.51 mg cm^{-2}, GSMs-H maintains a high reversible capacity of 818 mA h g^{-1}, indicating potential for real application. We also prepared GSMs-H with different sizes, the microcapsules with a diameter of 28 μm present 999 mA h g^{-1} when cycling at 0.2C. GSMs-H with a diameter of 117 μm shows 855 mA h g^{-1} after 50 cycles (Fig. S16, ESI†), which can be attributed to the excessively large size and the structural collapse caused by volume expansion during the cycling.

CV profiles at different rates are presented in Fig. 4a, e, and i. Although the CV curves of the three samples have a similar shape, a peak shift indicates an increasing polarization at high rates. GSMs-H presents the smallest shift for all three redox peaks, implying good kinetics for Li$^+$ ion transport.[46] Fig. 4b, f, and j show the relationship of log(i) *vs.* log(v) plots for the composites from equations $i = av^b$ and $\log(i) = b\log(v) + \log(a)$.[47] The b values for cathodic and anodic current peaks indicate a large charge contribution from a diffusion process.[48] In $i = k_1v + k_2v^{1/2}$, the k_1v and $k_2v^{1/2}$ represent the surface capacitive contribution and diffusion contribution, respectively.[49] The results are summarized in Fig. 4c, g, and k. The diffusion coefficient of Li$^+$ ions was studied using the CV curves. It is noted that the

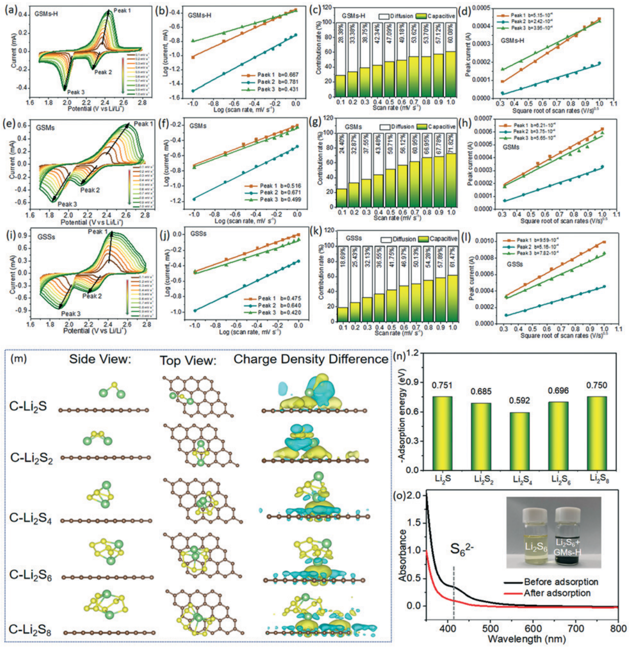

Fig. 4 CV curves of (a) GSMs-H, (e) GSMs, and (i) GSSs at different rates. Plots of log(i) *vs.* log(v) of these three cathodes based on (b) GSMs-H, (f) GSMs, and (j) GSSs. Contribution ratios at various rates for (c) GSMs-H, (g) GSMs, and (k) GSSs. The relationship between the peak currents and rates of (d) GSMs-H, (h) GSMs, and (l) GSSs. (m) DFT adsorption models between carbon and polysulfides, and the charge density difference of carbon with polysulfides. (n) Corresponding adsorption energies. (o) UV-vis absorption spectra of Li_2S_6 solution before and after the adsorption by GMs-H. Optical photographs show the color change of the solution.

linear relationship (Fig. 4d, h, and l) can be obtained by the Randles–Sevcik equation: $I_p = (2.69 \times 10^5) \cdot n^{1.5} A D_{Li^+}{}^{0.5} C_{Li^+} v^{0.5}$,[50] where I_p is the peak current (A), n is the number of electrons transferred during the redox reaction process (n = 2), A is the active electrode area, D_{Li^+} is the diffusion coefficient (cm^2 s^{-1}), C_{Li^+} is the concentration of Li ions in electrolyte, and v is the scan rate (V s^{-1}). The values of D_{Li^+} of peak 1, peak 2, and peak 3 of GSMs-H are 3.59×10^{-13}, 0.79×10^{-13}, 2.11×10^{-13} cm^2 s^{-1}, respectively, which are competitive.

To further investigate the immobilization capability towards polysulfides, we calculated the adsorption energies between carbon and a series of polysulfides. The optimized structures including top and side views are shown in Fig. 4m. The polysulfides are prone to adsorption with Li atoms being in contact with carbon atoms, whereas the sulfur is far away from the substrate. The results indicate the formation of Li–C bonds after electron transfer. The adsorption energies between carbon and Li_2S, Li_2S_2, Li_2S_4, Li_2S_6, and Li_2S_8 are −0.751, −0.685, −0.592, −0.696, and −0.750 eV (Fig. 4n), respectively, displaying immobilization capability towards polysulfides. In addition, the charge transfer density is presented in Fig. 4m. The yellow area represents the charge accumulation, and the blue area signifies the charge depletion. Obviously, the charge flows into the Li–C contact region to participate in bond formation. This indicates that the effectiveness of the microcapsule structure is helpful for suppressing the shuttle effect. The DFT calculations are supported further by adsorption measurements. In the inset of Fig. 4o, a distinct colour change of the Li_2S_6 solution from primrose yellow to transparent is observed after adding GMs-H, revealing strong anchoring towards polysulfides. Corresponding changes are further observed in the UV-vis spectra. After adsorption, the characteristic peak of S_6^{2-} species (410 nm) almost disappears,[51] indicating the strong adsorption capability of GMs-H due to the 3D GO scaffold inside and abundant functional groups on it, which are able to immobilize the polysulfides and enable good capacity retention during long-term cycling.

4. Conclusions

In summary, we present a GO scaffold-encapsulated microcapsule system for high-performance Li–S batteries, which is prepared through the CFF approach. After freeze-drying, the GO solution inside the microcapsule becomes a GO scaffold. The microcapsules are adjusted by changing the microfluidic rates. The prepared microcapsules deliver a high capacity of 1004 mA h g^{-1} at 0.2C after cycling 200 times, good rate-performance and long-term cycling stability during 1000 cycles at 2C. The batteries are also stable at −5 °C and 45 °C. The DFT calculations show the high adsorption energies of the microcapsules towards polysulfides including Li_2S, Li_2S_2, Li_2S_4, Li_2S_6, and Li_2S_8, indicating their capability for suppressing the shuttle effect. The microcapsule composites presented here with high electrochemical performance would enable them to be applied for preparing high-performance energy-storage materials and battery systems. This study provides a CFF method for one-step preparation of uniform-sized microcapsules with a solid shell and spherical shape at a high yield, which is feasible for various applications, such as microreactors, encapsulating drugs, medicine and pharmacy. In the future, it is expected that more studies are needed, such as improving the content of active materials inside the capsules, preparing small-size microcapsules, and demonstrating the detailed mechanism of interface chemistry for different core–shell microcapsule systems.

Conflicts of interest

There are no conflicts to declare.

Acknowledgements

This work was supported by the National Key Research and Development Program of China (2021YFC2100100), the Key Research and Development Program of Wuhu (2019YF07), the National Natural Science Foundation of China (21901157 and 11722222), and the Youth Innovation Promotion Association of CAS (2018491).

References

1 A. Manthiram, Y. Fu, S. Chung, C. Zu and Y.-S. Su, *Chem. Rev.*, 2014, **114**, 11751–11787.
2 Y. Li, S. Lin, D. Wang, T. Gao, J. Song, P. Zhou, Z. Xu, Z. Yang, N. Xiao and S. Guo, *Adv. Mater.*, 2020, **32**, 1906722.
3 Y. Song, W. Cai, L. Kong, J. Cai, Q. Zhang and J. Sun, *Adv. Energy Mater.*, 2020, **10**, 1901075.
4 Y. Li and S. Guo, *Matter*, 2021, **4**, 1142–1188.
5 S. Li and Z. Fan, *Energy Storage Mater.*, 2020, **34**, 107–127.
6 Y. Chen, T. Wang, H. Tian, D. Su, Q. Zhang and G. Wang, *Adv. Mater.*, 2021, **33**, 2003666.
7 Y. Wang, X. Huang, S. Zhang and Y. Hou, *Small Methods*, 2018, **2**, 1700345.
8 A. Bhargav, J. He, A. Gupta and A. Manthiram, *Joule*, 2020, **4**, 285–291.
9 R. Liu, W. Liu, Y. Bu, W. Yang, C. Wang, C. Priest, Z. Liu, Y. Wang, J. Chen and Y. Wang, *ACS Nano*, 2020, **14**, 17308–17320.
10 W. Ren, L. Xu, L. Zhu, X. Wang, X. Ma and D. Wang, *ACS Appl. Mater. Interfaces*, 2018, **10**, 11642–11651.
11 H. Liu, Z. Chen, L. Zhou, K. Pei, P. Xu, L. Xin, Q. Zeng, J. Zhang, R. Wu, F. Fang, R. Che and D. Sun, *Adv. Energy Mater.*, 2019, **9**, 1901667.
12 Y. Liu, W. Kou, X. Li, C. Huang, R. Shui and G. He, *Small*, 2019, **15**, 1902431.
13 M. Zhao, Y.-Q. Peng, B.-Q. Li, X.-Q. Zhang and J.-Q. Huang, *J. Energy Chem.*, 2021, **56**, 203–208.
14 S. Chen, J. Luo, N. Li, X. Han, J. Wang, Q. Deng, Z. Zeng and S. Deng, *Energy Storage Mater.*, 2020, **30**, 187–195.
15 J. Xie, Y.-W. Song, B.-Q. Li, H.-J. Peng, J.-Q. Huang and Q. Zhang, *Angew. Chem.*, 2020, **59**, 22150–22155.

16 A. Rashid, X. Zhu, G. Wang, C. Ke, S. Li, P. Sun, Z. Hu, Q. Zhang and L. Zhang, *J. Energy Chem.*, 2020, **49**, 71–79.

17 W. Wu, X. Li, L. Liu, X. Zhu, Z. Guo, W. Guo, Q. Han, J. He and Y. Zhao, *J. Mater. Chem. A*, 2022, **10**, 1433–1441.

18 G. Chen, Y. Li, W. Zhong, F. Zheng, J. Hu, X. Ji, W. Liu, C. Yang, Z. Lin and M. Liu, *Energy Storage Mater.*, 2020, **25**, 547–554.

19 Y. Lu, J. L. Qin, T. Shen, Y. F. Yu, K. Chen, Y. Z. Hu, J. N. Liang, M. X. Gong, J. J. Zhang and D. L. Wang, *Adv. Energy Mater.*, 2021, **11**, 2101780.

20 W. Li, X. Jin, L. Xiao, X. Li, Q. Xu, J. Weng and J. Xu, *J. Mater. Chem. A*, 2021, **9**, 26051–26060.

21 Z. Yu, M. Liu, D. Guo, J. Wang, X. Chen, J. Li, H. Jin, Z. Yang, X. A. Chen and S. Wang, *Angew. Chem.*, 2020, **59**, 6406–6411.

22 T. Yang, J. Xia, Z. H. Piao, L. Yang, S. C. Zhang, Y. L. Xing and G. M. Zhou, *ACS Nano*, 2021, **15**, 13901–13923.

23 I. Tantis, A. Bakandritsos, D. Zaoralova, M. Medved, P. Jakubec, J. Havlakova, R. Zboril and M. Otyepka, *Adv. Funct. Mater.*, 2021, **31**, 2101326.

24 J. Cao, C. Chen, Q. Zhao, N. Zhang, Q. Lu, X. Wang, Z. Niu and J. Chen, *Adv. Mater.*, 2016, **28**, 9629.

25 A. M. Ganan-Calvo, *Phys. Rev. Lett.*, 1998, **80**, 285.

26 T. Si, F. Li, X. Y. Yin and X. Z. Yin, *J. Fluid Mech.*, 2009, **629**, 1–23.

27 Z. Zhu, T. Si and R. X. Xu, *Lab Chip*, 2015, **15**, 646–649.

28 Q. Wu, C. Yang, G. Liu, W. Xu, Z. Zhu, T. Si and R. X. Xu, *Lab Chip*, 2017, **17**, 3168–3175.

29 G. Liu, Q. Wu, P. Dwivedi, C. Hu, Z. Zhu, S. Shen, J. Chu, G. Zhao, T. Si and R. X. Xu, *ACS Biomater. Sci. Eng.*, 2018, **4**, 3177–3184.

30 Z. Zhu, Q. Wu, S. Han, W. Xu, F. Zhong, S. Yuan, P. Dwivedi, T. Si and R. X. Xu, *Sens. Actuators, B*, 2018, **275**, 190–198.

31 Q. Wu, C. Yang, G. Liu, W. Xu, Z. Zhu, T. Si and R. X. Xu, *Lab Chip*, 2017, **17**, 3168–3175.

32 N. Wang, J. Wang, J. Zhao, J. Wang, J. Pan and J. Huang, *J. Alloys Compd.*, 2021, **851**, 156832.

33 X. Zhou, J. Tian, Q. J. Hu and C. Li, *Energy Storage Mater.*, 2020, **24**, 644–654.

34 X. Lin, J. Liu, H. Zhang, Y. Zhong, M. Zhu, T. Zhou, X. Qiao, H. Zhang, T. Han and J. Li, *Adv. Sci.*, 2021, **8**, 2002298.

35 B. Shao and I. Taniguchi, *Electrochim. Acta*, 2014, **128**, 156–161.

36 F. Zhong, C. Yang, Q. Wu, S. Wang, L. Cheng, P. Dwivedi, Z. Zhu, T. Si and R. X. Xu, *Int. J. Polym. Mater. Polym. Biomater.*, 2020, **69**, 840–847.

37 Z. Zhu, T. Si and R. X. Xu, *Lab Chip*, 2015, **15**, 646–649.

38 P. Geng, L. Wang, M. Du, Y. Bai, W. Li, Y. Liu, S. Chen, P. Braunstein, Q. Xu and H. Pang, *Adv. Mater.*, 2021, 2107836.

39 M. Du, X. Wang, P. Geng, Q. Li, Y. Gu, Y. An and H. Pang, *Chem. Eng. J.*, 2021, **420**, 130518.

40 Y. Yan, P. Zhang, Z. Qu, M. Tong, S. Zhao, Z. Li, M. Liu and Z. Lin, *Nano Lett.*, 2020, **20**, 7662–7669.

41 P. Chen, Z. Wu, T. Guo, Y. Zhou, M. Liu, X. Xia, J. Sun, L. Lu, D. X. Ouyang and X. Wang, *Adv. Mater.*, 2021, **33**, 2007549.

42 M. F. Zhu, C. Y. Yang, T. L. Han, C. Q. Hu, Y. Wu, T. Si and J. Y. Liu, *Mater. Chem. Front.*, 2021, **5**, 4565–4570.

43 X. Wang, D. Wang, C. Ma, Z. Yang, H. Yue, D. Zhang and Z. Sun, *Chem. Eng. J.*, 2022, **427**, 131622.

44 M. S. Kim, B. H. Lee, J. H. Park, H. S. Lee, W. H. Antink, E. Jung, J. Kim, T. Y. Yoo, C. W. Lee, C. Y. Ahn, S. M. Kang, J. Bok, W. Ko, X. Wang, S.-P. Cho, S. H. Yu, T. Hyeon and Y. E. Sung, *J. Am. Chem. Soc.*, 2020, **142**, 13406–13414.

45 L. Ding, C. Zhang, T. Wu, F. Yang, F. Lan, Y. Cao and M. Xiang, *J. Power Sources*, 2020, **466**, 228300.

46 B. Guan, Y. Zhang, L. Fan, X. Wu, M. Wang, Y. Qiu, N. Zhang and K. Sun, *ACS Nano*, 2019, **13**, 6742–6750.

47 K. Yao, Z. Xu, M. Ma, J. Li, F. Lu and J. Huang, *Adv. Funct. Mater.*, 2020, **30**, 2001484.

48 Y. Fang, D. Luan, Y. Chen, S. Gao and X. Lou, *Angew. Chem.*, 2020, **59**, 7178.

49 J. Y. Liu, M. F. Zhu, Z. H. Shen, T. Si, C. Q. Hu and H. G. Zhang, *Small*, 2021, **17**, 2103051.

50 H. Yamin, A. Gorenshtein, J. Penciner, Y. Sternberg and E. Peled, *J. Electrochem. Soc.*, 1988, **135**, 1045.

51 Y. Zhang, P. Zhang, B. Li, S. Zhang, K. Liu, R. Hou, X. Zhang, S. R. P. Silva and G. Shao, *Energy Storage Mater.*, 2020, **27**, 159–168.